

# Low light illumination study on commercially available homojunction photovoltaic cells



Johnny Russo<sup>a,\*</sup>, William Ray II<sup>a,b</sup>, Marc S. Litz<sup>a</sup>

<sup>a</sup> Sensors and Electron Devices Directorate, U.S. Army Research Laboratory, Adelphi, MD 20783, United States

<sup>b</sup> Oak Ridge Associated Universities (ORAU), Oak Ridge, TN 37831, United States

## HIGHLIGHTS

- COTS PV cells are tested under indoor and narrow light spectra.
- InGaP is the most efficient under low light conditions ( $0.5\text{--}100\ \mu\text{W}_{\text{opt}}/\text{cm}^2$ ).
- InGaP is selected for isotope battery.
- Optimal incident wavelength (614 nm) for InGaP is identified in model.

## ARTICLE INFO

### Article history:

Received 11 September 2016

Received in revised form 9 January 2017

Accepted 14 January 2017

Available online 28 January 2017

### Keywords:

Low light illumination

Photovoltaic cells

InGaP

GaAs

Homojunction commercially available

## ABSTRACT

Low illumination ( $10^{-4}$  suns) and indoor light energy harvesting is needed to meet the demands of zero net energy (ZNE) building, Internet of Things (IoT), and beta-photovoltaic energy harvesting systems to power remote sensors. Photovoltaic (PV) solar cells under low intensity and narrow ( $\pm 40$  nm) light spectrum conditions are not well characterized nor developed, especially for commercially available devices and scalable systems. PV operating characteristics under 1 sun illumination decrease at lower light intensity and narrow spectrum conditions (efficiency drops from  $\sim 25\%$  at  $100\ \mu\text{W}_{\text{opt}}/\text{cm}^2$  to  $2\%$  at  $1\ \mu\text{W}_{\text{opt}}/\text{cm}^2$ ). By choosing a PV with a bandgap that matches the light source operating wavelength, the total system efficiency can be improved. By quantifying losses on homojunction photovoltaics (thermalization and leakage current), we have determined the theoretical optimized efficiency for a set of PV material and a selected set of light sources. We measure single-junction solar cells' parameters under three different light sources (indoor light and narrow spectrum LED sources) with light intensities ranging from  $0.5$  to  $100\ \mu\text{W}_{\text{opt}}/\text{cm}^2$ . Measurements show that indium gallium phosphide (InGaP) PV has the highest surface power density and conversion efficiency ( $29\%$  under  $\approx 1\ \mu\text{W}_{\text{opt}}/\text{cm}^2$  from a  $523$  nm central peak LED). A beta-photovoltaic experimental study identifies InGaP to be optimized for use with the ZnS:Cu, Al and tritium at STP. The results have guided the selection of PV material for scalable isotope batteries and other low-light energy harvesting systems.

Published by Elsevier Ltd.

## 1. Introduction

Autonomous systems and sensors have been rapidly increasing in use and importance for commercial environmental monitoring, as well as residential applications, and commercial applications over the past decade [1,2]. This growth in popularity of independent, wireless systems and sensors has led to rise of the Internet of Things (IoT) [3]. They are embedded in home appliances, outdoor weather stations, and remote monitoring system of physical

characteristics and events. Presently, to increase sensor lifetime and independence from the primary grid most sensors have standby/sleep modes at low power consumption ranging from  $1\ \text{nW}_e$  to  $1\ \mu\text{W}_e$  (Fig. 1), and shift into dynamic/wakeup mode from an external environmental stimulus or remote user command [4–7]. Yet, this does not solve the limiting factor for energy storage for a lengthy operation of 10 years or longer. Most wireless sensor networks (WSNs) for outdoor and indoor applications use chemical batteries, especially since indoor conditions limit energy harvesting opportunities. Commercial chemical batteries have storage lifetimes of less than a decade when stored under standard conditions even when unused. In order for the IoT to be more successful and grow, thousands of unattended, embedded systems and sensors

\* Corresponding author.

E-mail addresses: [john.a.russo20.civ@mail.mil](mailto:john.a.russo20.civ@mail.mil) (J. Russo), [william.b.ray32.ctr@mail.mil](mailto:william.b.ray32.ctr@mail.mil) (W. Ray II), [marc.s.litz.civ@mail.mil](mailto:marc.s.litz.civ@mail.mil) (M.S. Litz).

### Nomenclature

a-Si	amorphous silicon	LPV	laser power converter or photovoltaic
ARL	US Army Research Laboratory	mc-Si	monocrystalline silicon
$\beta$ -PV	beta-photovoltaic	MJ	multi-junction
CL	cathodoluminescence	MPP	maximum power point
DSC	dye-sensitized solar cells	NPRL	NanoPower Research Labs
$E_g$	bandgap of semiconductor device	OPV	organic photovoltaic
$E_{ph}$	incident photon energy	$P_{in}$	input power of light source
$E$	total power density of visible EM radiation	PV	photovoltaic
EQE	external quantum efficiency	QE	quantum efficiency
EM	electromagnetic	$R_s$	series resistance
FF	fill factor	$R_{sh}$	shunt resistance
FWHM	full width at half maximum	RF	radio frequency
GaAs	gallium arsenide	RL	radioluminescence
IDEC	indirect energy conversion	RIT	Rochester Institute of Technology
iBAT	isotope battery or radioisotope battery	RPD	radiant power density
$I_0, I_d$	dark current	$S_e$	specific power density
$I_{sc}, I_g$	short circuit current	STC	standard test conditions
InGaP	indium gallium phosphide	STP	standard temperature and pressure
IR	infrared	TL	thermalization loss
IoT	internet of things	$V_{oc}$	open circuit voltage
$I$ - $V$	current-voltage	$V_m$	voltage of the maximal power point
$J_{sc}$	short circuit current density	WSN	wireless sensor network
LIL	low illumination light	ZNE	zero net energy

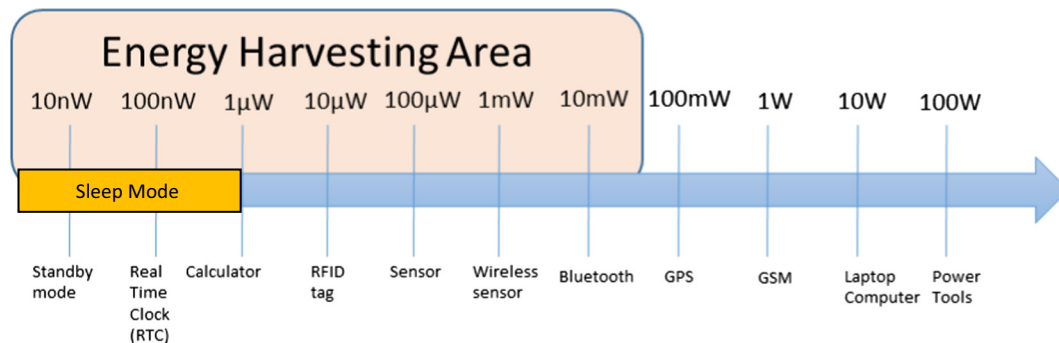


Fig. 1. Power levels for portable electronic devices and correlated energy harvesting capabilities [54].

would need to be spread everywhere: indoor and outdoor environments, remote and urban, terrestrial and aquatic. They may be located in harsh and remote locations, where replacing many batteries can be inefficient, and otherwise difficult without established logistic lines. The need for a blanket of sensors and systems and their replacements generate complex logistic chains and large labor costs. The ultimate goal is to establish an energy harvester system that can provide power to an autonomous system or sensor without use of energy storage. If autonomous sensors can be developed to harvest ambient energy, the WSN operation lifetime could last beyond the infrastructure lifespan or be limited to only the ambient energy source lifetime, such as with a radioisotope battery system. Indoor and other low-light energy harvesting photovoltaic cells (PVs) can power autonomous sensors similar to outdoor systems. Artificial lighting is constantly radiating during daily facility operation at a constant peak intensity unlike outdoor solar lighting. Indoor light energy harvesting could meet and satisfy demands of Net Zero Building Systems (ZNE) [8]. This would be beneficial for power recycling programs since indoor lighting is 25% of facility power consumption [9].

Indoor photovoltaic (IPV) systems' need to operate in conditions that are not standard, but diverse due to different light spectra and

intensities ( $W_{opt}/cm^2$ ). Muller [10], Randall [11], and Roundy [12] have presented indoor lighting models using office space lighting values where the light spectrum was fixed following artificial lighting and the light intensity was varied. The light intensity in the model changes with respect to time of day, month in the year, and room location, e.g. middle of room or near office window. These models only include silicon PV types and mixed lighting conditions based on CFL, incandescent, and solar light spectrum excluding UV light. Previous work on silicon (Si) PVs, dye-sensitized solar cells (DSC), and organic photovoltaics (OPVs) using the indoor light model conditions have been characterized for indoor light harvesting by Steim [13], Sacco [14], De Rossi [15], and Corazza et al. [16]. Sacco et al. [14] measured OPV, DSC, and Si PVs under artificial illumination conditions, using incandescent, halogen, and fluorescent bulbs. DSC and silicon spherical and crystalline micro-cells (Si- $\mu$ sph) showed the highest power conversion efficiency of 4.41% and 5.89% at 5000 lx. De Rossi et al. [15] showed that an optimized DSC outperforms silicon PV devices under CFL and warm white LED. The power conversion efficiency of DSC is approximately 13% at 200 lx [15]. PCDTBT was found to be the most promising OPV with an efficiency of 16.6% at 300 lx from a fluorescent lamp [17]. In general, these papers suggest that DSC

and OPVs are the best IPVVs under artificial illumination conditions. There are missing elements and conditions with these models that have not been investigated on IPV systems such as lower light intensity, additional light spectra, and additional homojunction PV cells. Other common PV types like GaAs and InGaP have been measured under CFL and LED illumination [18]. Published work on GaAs and InGaP measured below an indoor and narrow spectrum intensity of  $29 \mu\text{W}_{\text{opt}}/\text{cm}^2$  has not been achieved.

PVs can be used to convert other light sources that are even lower in intensity with a narrower spectrum when compared to indoor lighting. They can support autonomous systems without a high quantity of energy storage. Remote systems located in concealed areas where there are no external energy stimuli to harvest require a high-energy dense energy source with minimal volume. Radioisotope batteries can fulfill these qualifications, providing electrical energy for an operation lifetime of multiple decade. They are divided into two main groups: betavoltaic ( $\beta\text{V}$ ) and betaphotovoltaic ( $\beta\text{-PV}$ ) cells. A  $\beta\text{V}$  cell is based on electron-hole pair (EHP) creation in the ionization trails of high-energy electrons from radioisotope beta particles colliding in a semiconductor. A  $\beta\text{-PV}$  cell is a two-step conversion process converting first the kinetic energy from nuclear beta decay to optical light energy in a phosphor, then optical to electrical energy conversion through the photoelectric effect using a PV [19,20]. Characterized IPVVs can be used in the  $\beta\text{-PV}$  cell to convert the low light illumination from phosphor radioluminescence emission. The phosphor represents an energy conversion medium of lower mass density [19].  $\beta\text{-PV}$  cells lower internal and external interaction losses within and on the surface of the semiconductor by converting high-energy beta particles into photons by luminescence and phosphorescence processes [21]. The phosphor as an additional energy conversion step lowers the  $\beta\text{-PV}$  energy density as compared to a  $\beta\text{V}$ , as well as introducing losses between the photon emission and PV. Thermalization loss occurs when the incoming photon does not match the PV bandgap which can be considered a major loss factor when the photon flux is low compared to indoor lighting and global AM1.5G standard testing conditions (STC). Matching phosphor emission wavelength to PV bandgap needs to be done to increase overall power conversion efficiency.

This report investigates PV cells for IPV applications. The report focuses on identifying PV losses under low light, narrow-spectrum conditions along with the influence of specific light sources on four PV cell types. Intrinsic material defects from material growth along with packaging processes such as epoxies and passivation can generate additional losses. Leakage, or dark, current ( $I_0$ ), increases “noise” level and is a byproduct of these fabrication losses. These increases in background “noise” are particularly noticeable under low light conditions where less efficient photocurrent generation is measured, along with reduced voltage operating point during less than 1 sun illumination. Shunt resistance ( $R_{sh}$ ) is another important parameter for low light intensity applications [22,23]. This parasitic resistance originates from bulk effects, causing power dissipation in the PV by allowing alternative current paths for the photon-generated electron hole pairs (EHPs). Higher  $R_{sh}$ , calculated from  $I$ - $V$  leakage curve slope at low voltage, increases overall PV efficiency under low light and standard conditions. Quantum efficiency, thermalization losses (TLs), and below bandgap ( $E_g$ ) losses of incoming light are considered as fundamental and unavoidable losses [24–27]. PV external quantum efficiency (EQE) from product datasheets and other creditable research work on the tested devices are referenced. The work in this paper is limited to one indoor light spectrum and two narrow spectral emission to simulate phosphor radioluminescence (RL) and cathodoluminescence (CL): cool white, blue, and green light-emitting diodes (LEDs). PV short circuit current density ( $J_{sc}$ ), open

circuit voltage ( $V_{oc}$ ),  $I_0$ , fill factor (FF), and power conversion efficiency ( $\eta$ ) are measured for each light source and compared to STC results. Furthermore, the PV cell type for use in a  $\beta\text{-PV}$  isotope battery (iBAT) is identified [28,29]. Finally, a model is developed to identify the optimal wavelength for the highest power conversion efficiency of a homojunction-type PV cell. Thermalization, absorption losses, and external quantum efficiency are included in the model to calculate the PV ideal conversion efficiency at each incident photon energy.

## 2. Experimental setup

### 2.1. PV devices

Four PV devices ( $1 \times \text{InGaP}$ ,  $1 \times \text{GaAs}$ ,  $1 \times \text{a-Si}$ , and  $1 \times \text{mc-Si}$ ) are selected to determine a suitable candidate for low-light energy harvesting for indoor light ( $50\text{--}1000 \mu\text{W}_{\text{opt}}/\text{cm}^2$ ) and scintillation light from phosphors ( $0.5\text{--}4 \mu\text{W}_{\text{opt}}/\text{cm}^2$ ). The typical operating conditions for PV devices is the outdoor lighting dominated by the solar spectrum with a range of  $200\text{--}2500 \text{ nm}$  and a radiant power density of  $100 \text{ mW}_{\text{opt}}/\text{cm}^2$ . The PV characteristics under STC 1 sun AM 1.5 are shown in Table 1. Microlink Devices Inc. [30] and NanoPower Research Laboratory at Rochester Institute of Technology (RIT) [31] measured GaAs and InGaP cells under STC (Table 1). Both are grown using MOCVD. The a-Si PV cell is a CBC-PV-02 Cymbet solar cell [32]. The mc-Si PV cell is an IXYS product [33]. Similar to the previous homojunction PV cells,  $J_{sc}$ ,  $V_{oc}$ , FF, and  $\eta$  were measured under STC by the two companies (Table 1). They are all commercially available for energy recycling commercial and government initiatives. The PV EQE are shown in Fig. 2. The peak EQE for the monocrystalline Si and GaAs are  $\sim 700 \text{ nm}$ , while the InGaP peak EQE is  $\sim 540 \text{ nm}$ . The InGaP EQE is measured and compared to specification sheets from manufacturer for all others. Leakage current ( $I_0$ ) is measured by the HP 4155B semiconductor parameter analyzer. The true leakage current of the PV devices should be a few orders magnitude lower ( $10^{-3}$ ) than measured value. The measurement is limited by the parameter analyzer sensitivity and resolution.

### 2.2. Light sources and spectra

PV devices are characterized under low-light illumination: cool white LED, blue and green LED, and monochromator. All low-light illumination is between  $400$  to  $750 \text{ nm}$  with different radiant power densities (RPD). Three light sources (LEDs from CREE and HLMP brands) are selected to simulate indoor light and phosphor RL from beta-emitting radioisotopes. The two colored LED are selected for testing because their light spectra of  $470 \pm 30 \text{ nm}$  and  $523 \pm 47 \text{ nm}$  match closely with the most efficient phosphors that commercially available, ZnS:Ag ( $E_\lambda = 440 \text{ nm}$ ) and ZnS:Cu,Al ( $E_\lambda = 530 \text{ nm}$ ). The indoor light spectrum is dependent on the specific light source and reflected and diffused light in the closed space. Typical indoor spectrum is from  $400$  to  $700 \text{ nm}$  with the largest portion between  $450$  and  $600 \text{ nm}$ . Although indoor lighting is lower in intensity than solar lighting, indoor irradiance is higher than solar in the visible spectrum when both light spectra's RPD, also called total power density  $E$ , are normalized ( $\Sigma \approx 0.1 \text{ mW}_{\text{opt}}/\text{cm}^2$ ), shown in Eq. (1).

$$PD = E = \int_0^\infty E_\lambda(\lambda) \cdot d\lambda \quad (1)$$

This parameter is considered light intensity in this report [24]. The solar light intensity is normalized through multiplication by a factor of  $0.001$ , from  $88 \text{ mW}_{\text{opt}}/\text{cm}^2$  to  $0.088 \text{ mW}_{\text{opt}}/\text{cm}^2$ . Normalized solar light intensity is calculated by the summation of power

**Table 1**  
STC electrical characteristics of four commercial PV evaluated under low-light illumination.

PV type	Device surface area (cm <sup>2</sup> )	E <sub>g</sub> (eV)	Dark/leakage current density, J <sub>0</sub> (A/cm <sup>2</sup> )	R <sub>sh</sub> (Ω)	STC 1 Sun AM 1.5			
					J <sub>sc</sub> (mA/cm <sup>2</sup> )	V <sub>oc</sub> (V)	FF (%)	η (%)
GaAs	0.25	1.43	2.27E–10	2.0E+9	0.19 <sup>a</sup>	1.19 <sup>a</sup>	68.82 <sup>a</sup>	17 <sup>a</sup>
InGaP	1.2	1.86	1.49E–13	1.04E+10	14.4 <sup>b</sup>	1.35 <sup>b</sup>	83 <sup>b</sup>	16.5 <sup>b</sup>
a-Si	17	1.1–1.5 <sup>c,d,**</sup>	3.52E–10	2.02E+06	16.4 <sup>c</sup>	0.896 <sup>c</sup>	63 <sup>c</sup>	10.2 ± 0.3 <sup>c</sup>
mc-Si	1.3	1.12 <sup>f</sup>	8.62E–12	4.75E+06	42.4 <sup>g</sup>	>0.696 Max. 1.89 <sup>g</sup>	>65 Max. 83.6 <sup>g</sup>	22–24.4 <sup>g</sup>

<sup>a</sup> Ref. [30].

<sup>b</sup> Ref. [31].

<sup>c</sup> Ref. [32].

<sup>d</sup> Ref. [58].

<sup>e</sup> Ref. [59].

<sup>f</sup> Ref. [60].

<sup>g</sup> Ref. [33].

<sup>\*\*</sup> The bandgap range of amorphous silicon at room temperature is from 1.1 eV to 1.95 eV depending on hydrogen content and alloy type [58].

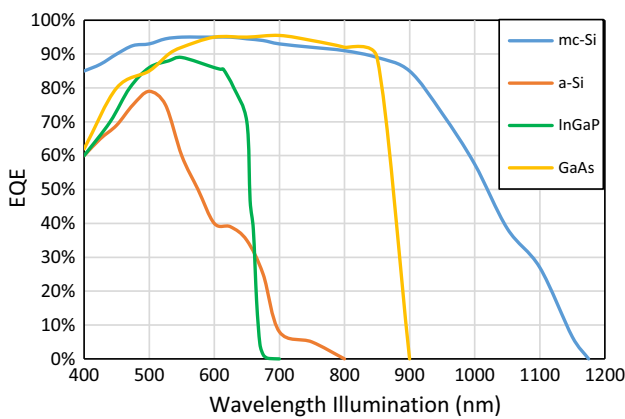


**Fig. 2.** EQE as a function of wavelength for PV tabulated in Table 1 [30–33].

density at each wavelength ( $\frac{W_{\text{opt}}}{\text{m}^2 \times \text{nm}}$ ) multiplied by a factor of 0.001. If both spectra are at the same magnitude such as 0.1 mW<sub>opt</sub>/cm<sup>2</sup>, the cool white LED has 57% more RPD than solar radiation in the visible spectrum (400–700 nm). Indoor lighting has a higher photon flux at visible light range compared to solar lighting. Solar UV and IR are excluded in this comparison. Fig. 3 shows the standard solar spectrum from 300 to 1200 nm compared to cool white light spectrum.

The optical power density of the light sources ranges from 0.5 to 100 μW<sub>opt</sub>/cm<sup>2</sup>. Actual indoor optical power density varies from 35 to 1000 μW<sub>opt</sub>/cm<sup>2</sup> depending on location and distance from light source and shadowing [34]. We have chosen a lower intensity range to represent the lower bound of indoor light conditions. Cool white LED (400–700 nm) is selected as the primary indoor simulator due to its increase commercial use and superiority over other typical light source with regard to lifetime, reliability, and overall energy efficiency from input electrical to output optical power [35]. Currently, there is no normal indoor light spectrum standard like those that exist for solar irradiance (AM 1.5, AM 1.0, etc.).

The Newport radiometer 818-UV model at a fixed distance from the light source measures the cool-white LED RPD. The calibration uncertainty without attenuator is 1% at 350–949 nm. Since the radiometer is designed to measure narrow spectrum light sources, light binning is necessary to measure the total optical power density, especially for the cool white light source. Calibrated bandpass filters from 400 to 700 ± 25 nm are individually placed over the top of the detector surface. The radiometer is set at the bandpass filter wavelength. The optical power density is recorded for each filter. All of the individual power densities ( $\frac{W_{\text{opt}}}{\text{m}^2 \times \text{nm}}$ ) are summed up to calculate RPD for each input power setting. Lastly, the bandpass

filters are removed and a median wavelength of the light spectrum is set on the radiometer to measure three optical power densities (1, 10, and 100 μW<sub>opt</sub>/cm<sup>2</sup>) at the three input power settings used in the binning procedure. The percent error is less than 3% when using the median wavelength calibration of 485-nm setting on the optical meter. This allows us to measure the white light source without needing to bin the incident white light in every PV I-V curve measurement. Fig. 4 shows images and an illustration of LED light intensity experiment and radiometer.

The colored LEDs closely simulate RL low-light intensities. The LED spectra (±15 nm) are narrower than the phosphors' spectra (±50 nm). As a result, PVs are more efficient in harvesting radiant energy under a narrower spectrum from LED compared to RL emission from a phosphor. The optical power meter's calibration factor is set at the central wavelength of the colored LED. The PVs are exposed to several light intensity points from 0.5 to 4 μW<sub>opt</sub>/cm<sup>2</sup> to determine the PV conversion efficiency values and characteristics change under extremely low-light conditions. The phosphor optical power density is 0.5 ≥ P<sub>opt</sub> > 4 μW<sub>opt</sub>/cm<sup>2</sup>, depending on the beta-emitting radioisotope, beta flux, and phosphor RL/CL conversion efficiency [29,36,37].

One of the goals is to determine the light intensity, either blue or green, that will give us the largest PV electrical output for the specified intensity ranges. Narrowband LED and phosphor RL spectra with relative intensity are shown in Fig. 5. For further characterization of PV devices, a Princeton Instrument Acton SP2300 imaging triple monochromator is used to illuminate near single wavelengths on the device. The monochromator (440–700 nm) illuminates the PV cell that has the largest conversion efficiency from all wider spectrum light sources. The light source is used to find the optimal wavelength for maximum energy conversion of the absorber. The RPD of the device is 92 and 185 nW<sub>opt</sub> for each wavelength with a bandwidth less than a few nanometers from the central wavelength.

### 2.3. Illumination methods

LED intensity is controlled by a designated power supply and measured by the radiometer. PV device and radiometer are placed in two light-tight enclosure. Each LED is mounted to lid of light-tight enclosure, illuminating the PV and radiometer surface always positioned at the same distance of 5 cm from the PV surface. Radiometer's calibration setting is set to the light sources' central wavelength for each measurement. The PV device is connected to the parameter analyzer. I-V curve is measured for each light intensity measured by the radiometer. Fig. 6 shows an illustration of the method.

In addition, an automated (power level adjusted) monochromator is used to measure the PV current and EQE. The monochromatic

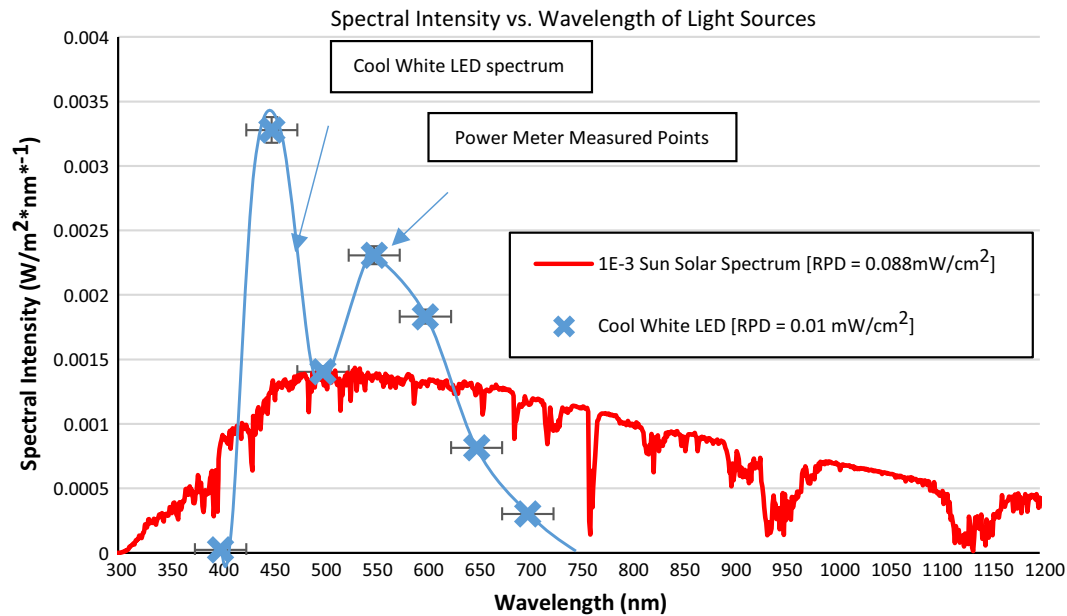


**Fig. 3.** Spectral intensity (irradiance) as a function of the incident photon wavelength comparing the cool white LED at an RPD of 0.01 mW<sub>opt</sub>/cm² to the 10<sup>−3</sup> sun global AM1.5G solar spectrum at 0.088 mW<sub>opt</sub>/cm². Bandwidth for the bandpass filters is ±25 nm (y-axis) shown by the error bars. The error for cool white LED at 0.01 mW<sub>opt</sub>/cm² is 3%, which includes the calibration uncertainty of Newport radiometer 818-UV model (x-axis).

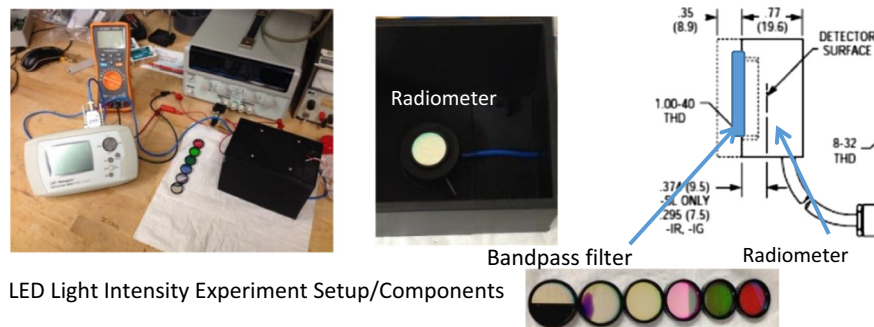


**Fig. 4.** Experimental setup showing a radiometer inside the light tight enclosure. Bandpass filters are placed on the top of the radiometer silicon detector head to bin the incident light for the cool white LED. Six measurements are taken for each bandpass filter, which covered the entire white LED spectrum range. For each measurement, the radiometer set wavelength is changed to the central wavelength of the bandpass filter.

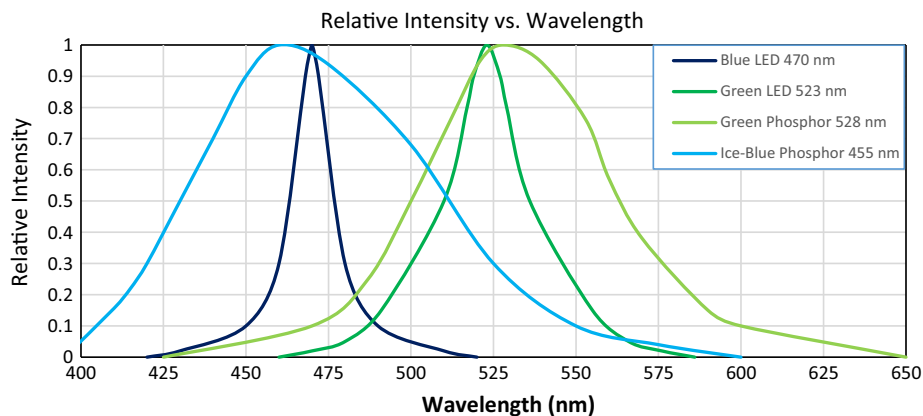


**Fig. 5.** LED spectra are used to simulated phosphors in device calibrations. LED spectra (±15 nm) are typically narrower than phosphor spectra (±45 nm). Relative intensity as a function of wavelength for green and blue LED (used in experimental measurements) are compared to the available phosphor RL emission options commercially available [55–57].



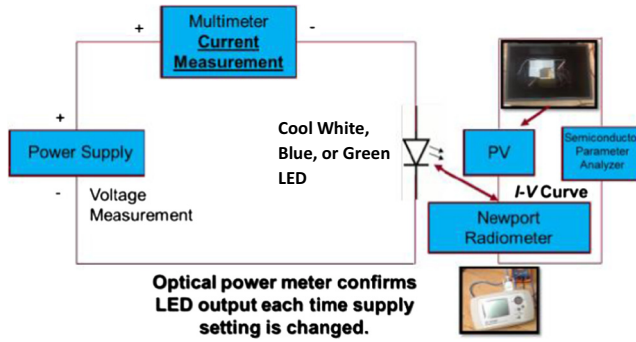


**Fig. 6.** Illustration of the LED illumination method. The optical power meter confirms the LED optical power density for every PV *I-V* curve trace on the semiconductor parameter analyzer. The radiometer surface and PV surface are both placed the same distance from the light source. Both devices are placed in light-tight enclosures.

source (a Princeton Instrument Acton SP2300) has FWHM of a few nanometers. Device is placed in light-tight enclosure. An optical power meter measures the radiant power densities of the monochromatic light for each wavelength at a constant distance. PV device is placed at this exact distance from the optical fiber cable shown in Fig. 7. Short-circuit current as a function of wavelength is measured from 440 to 700 nm for GaAs and InGaP (Fig. 7).

### 3. Results and discussion

PV devices are measured under the low-light illumination of three discrete LED light sources. Of the four PV devices measured, the device with the largest conversion efficiency is studied further by continuously varying the wavelength with a monochromator. Spectral response, EQE, and PV power conversion efficiency ( $\eta$ ) of InGaP cell are measured.

#### 3.1. Low-light illumination of PV using LEDs

Four PV material types are tested under the same conditions with respect to aperture size (1-cm<sup>2</sup>), illumination distance, and

intensities. *I-V* curves are measured for each PV under the illumination by three different light sources ranging from approximately 0.5–100  $\mu\text{W}_{\text{opt}}/\text{cm}^2$ .  $J_{\text{sc}}$ ,  $V_{\text{oc}}$ , maximum power point (MPP), surface power density ( $S_e$ ), power conversion efficiency ( $\eta$ ), and Fill Factor (FF) are measured and calculated. Table 2 compares PV conversion efficiency and FF for each light source at a RPD of 1  $\mu\text{W}_{\text{opt}}/\text{cm}^2$ .

Four light sources are compared in Fig. 8 for spectral irradiance as a function of wavelength. Overall, power conversion efficiency is higher under green illumination compared to the blue light (Table 2). This relationship holds true on FF,  $V_{\text{oc}}$ , and  $J_{\text{sc}}$  for the four PVs (Fig. 9). For example, the InGaP's FF increases only slightly for each light source (blue, green and white) from 0.5 to 100  $\mu\text{W}_{\text{opt}}/\text{cm}^2$ . Under green light illumination, InGaP FF stays constant at approximately 83% throughout the light intensity range because it has the lowest thermalization loss and leakage current. The InGaP leakage current is  $10^3$  lower than the other three PV samples (Table 1). Less PV photocurrent is dissipated in internal losses with high  $R_{\text{sh}}$  [14]. InGaP FF is expected to fall in a similar manner as observed in a-Si, mc-Si, and GaAs when the photocurrent is closer to the leakage current. Further work will be performed in future studies on  $V_{\text{oc}}$ ,  $J_{\text{sc}}$ , and FF losses under these three light sources at low light intensity range (1–500  $\text{nW}_{\text{opt}}/\text{cm}^2$ ). The PV  $V_{\text{oc}}$  and  $J_{\text{sc}}$  under these low light conditions will be compared. Overall, all four PV types have lower thermalization loss and higher EQE under green light. Thermalization losses between emitter and absorber significantly influence system conversion efficiency when both light emitters are equal in RPD, i.e., for InGaP,  $S_e$  (2.3 eV) = 0.24  $\mu\text{W}_e/\text{cm}^2$  and  $S_e$  (2.72 eV) = 0.13  $\mu\text{W}_e/\text{cm}^2$  at an input of 1  $\mu\text{W}_{\text{opt}}/\text{cm}^2$ . Both colored light sources simulate zinc sulfide-based phosphors' RL/CL emission at low intensity (RPD = 0.5–4  $\mu\text{W}_{\text{opt}}/\text{cm}^2$ ). Narrow spectrum and low-light results show that a more efficient phosphor (>2 $\eta$ ), will generate a higher system  $S_e$  under low light intensities (RPD  $\leq$  2  $\mu\text{W}_{\text{opt}}/\text{cm}^2$ ) because the PV electrical output overcomes the intrinsic leakage current losses.

All PV cells measure a large efficiency increase from 0.5 to 10  $\mu\text{W}_{\text{opt}}/\text{cm}^2$  [ $m_{\text{avg}} \approx 1\% / (\mu\text{W}_{\text{opt}}/\text{cm}^2)$  for InGaP] compared to a gradual increase from 10 to 100  $\mu\text{W}_{\text{opt}}/\text{cm}^2$  [ $m_{\text{avg}} \approx 0.13\% / (\mu\text{W}_{\text{opt}}/\text{cm}^2)$  for InGaP] for all light sources, refer to Figs. 10–12. The PV efficiency as a function of light intensity curves are qualita-

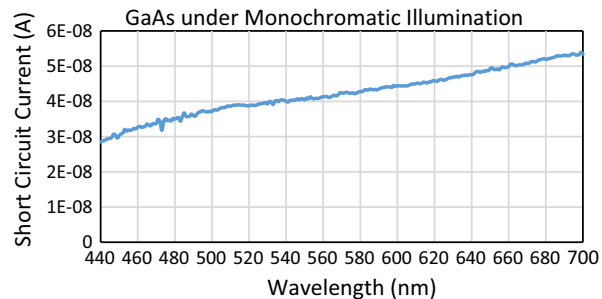
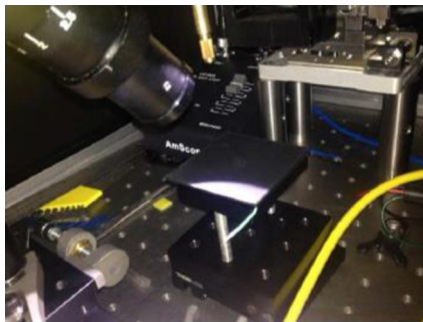


**Fig. 7.** Image of the monochromatic illumination setup (left) and GaAs short circuit current as function of wavelength at 185 nWopt operating point (right).

**Table 2**

PV power conversion efficiency ( $\eta$ ) and FF for the three experimental light sources performed at the same intensity (RPD  $\approx$  1  $\mu\text{W}_{\text{opt}}/\text{cm}^2$ ). The highest efficiency measured is the InGaP PV cell under 523 nm irradiation.

Light source (RPD $\approx$ 1 $\mu\text{W}_{\text{opt}}/\text{cm}^2$ )	523 nm		470 nm		Cool white LED (400–750 nm)	
	FF (%)	$\eta$ (%)	FF (%)	$\eta$ (%)	FF (%)	$\eta$ (%)
InGaP	84	29	63	13	61	15
GaAs	35	3.0	32	1.6	32	1.5
a-Si	26	1.6	26	1.3	26	1.5
mc-Si	50	0.95	47	0.9	43	2

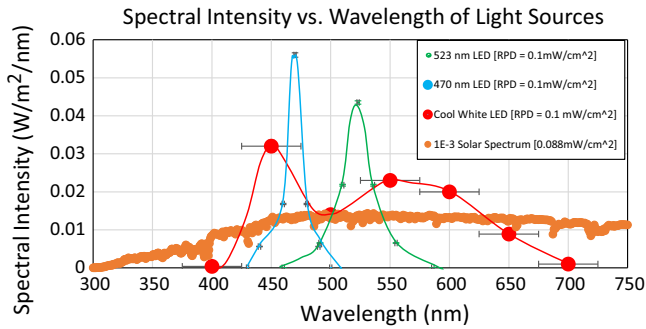


**Fig. 8.** Light spectra of the AM1.5G and illumination sources used in experimental evaluation are shown. All narrow spectrum light sources are at the same RPD ( $0.1 \text{ mW}_{\text{opt}}/\text{cm}^2$ ). The AM1.5G RPD is at  $0.088 \text{ mW}_{\text{opt}}/\text{cm}^2$ .

tively the same in shape for all three light sources (cool white, green and blue LEDs). The PV conversion efficiency divides into two light intensity (RPD) regimes:  $0.5 - 10 \mu\text{W}_{\text{opt}}/\text{cm}^2$  and  $10 - 100 \mu\text{W}_{\text{opt}}/\text{cm}^2$ . Conversion efficiency under the higher regime and solar spectrum is largely affected by the PV cell bandgap. The two loss mechanisms are thermalization and non-absorption losses from the incident photon energy [38]. For the solar spectrum, the ideal homojunction PV bandgap is 1.35 eV. GaAs ( $E_g = 1.43 \text{ eV}$ ) is the most efficient homojunction PV cell under

STC at 22.08% [39,40]. However, the results in Table 1 show that InGaP and GaAs have similar efficiencies, 16.5% and 17%, under STC even though their bandgaps are different. The tested GaAs sample has a lower measured  $\eta$  and FF due to loss mechanisms that culminate in parasitic resistances, which are device internal losses [38]. InGaP shunt and series resistance are  $10.4 \text{ G}\Omega$  and  $100 \Omega$ , and GaAs shunt and series resistance are  $2.0 \text{ G}\Omega$  and  $51.8 \Omega$ . The parasitic resistances counter and lower the GaAs bandgap advantage over InGaP caused by defects in the device and passivation layer type and quality. GaAs's anti-reflective coating (ARC) could have higher surface recombination rates and higher reflection percentage under STC [41]. These reasons are postulates since only the ARC type is known for each PV.

Internal losses' impact on PV conversion efficiency is greater under lower regime conditions, both narrow and solar spectrum, because the photocurrent is closer to device leakage current. The internal losses are divided into two categories: surface effects and bulk effects. Both loss mechanisms influence the PV cell leakage current density ( $J_0$ ) and  $R_{sh}$ .  $J_0$  and  $R_{sh}$  are not mentioned often in vendor technical documents because lower regime conditions are atypical. For surface effects, higher surface recombination rates on the top surface between the PV front contacts lowers  $J_{sc}$  and  $V_{oc}$ . To counter surface losses, surface recombination rates are lowered through passivation on the PV surface and heavy doping under front contacts [41]. Ruhle et al. investigated various passivating

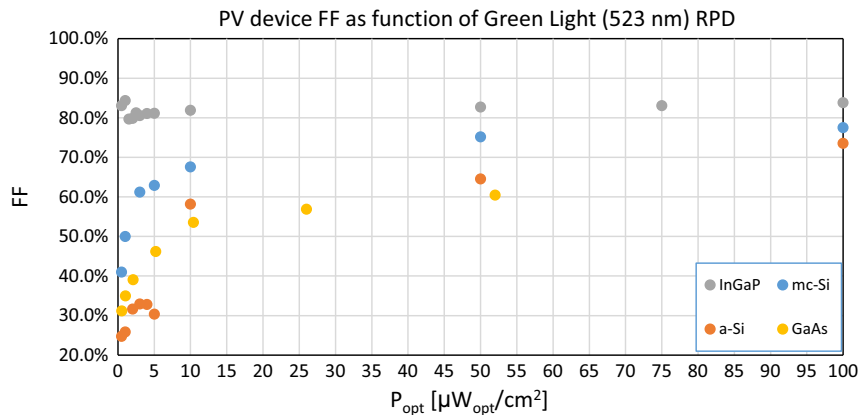


**Fig. 9.** PV FF as function of light intensity for green LED. (For interpretation of the references to color in this figure legend, the reader is referred to the web version of this article.)

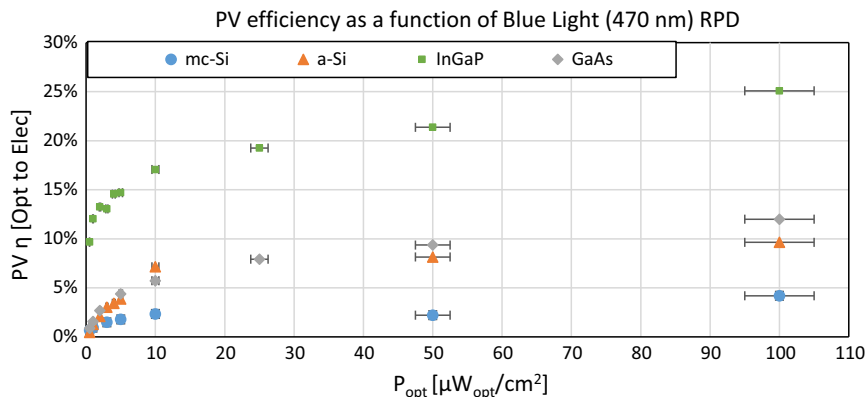


**Fig. 10.** PV conversion efficiency as function of light intensity for blue LED. Optical power density error is calculated using the optical power meter spectral response ( $SR(\lambda)$ ) and the full width at half maximum (FWHM) of the two LEDs: blue and green. The detector is measuring over the entire "broad" spectrum of the source, so the  $SR$  values of the two extreme FWHM value must be accounted for to calculate the optical power measurement error. The optical power error is 5%, which includes detector uncertainty. The electrical power measurement error is less than 1%. (For interpretation of the references to color in this figure legend, the reader is referred to the web version of this article.)

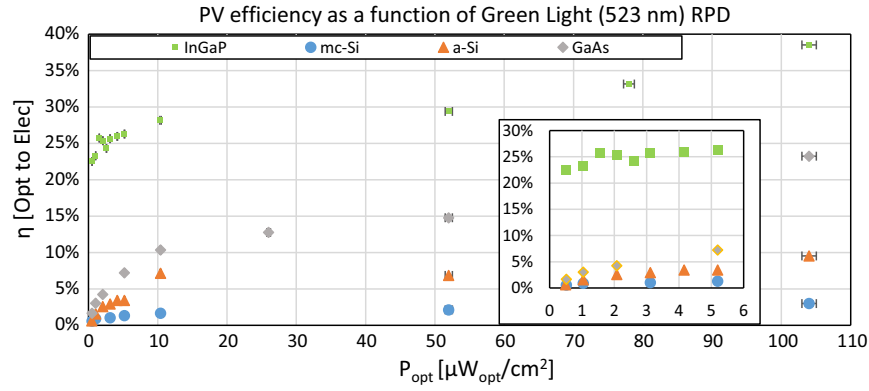


**Fig. 11.** PV conversion efficiency as function of light intensity for the green LED. The optical power error is 11% because the FWHM is wider than the blue light source. To reduce error, the detector spectral response curve is weighted to the light source spectrum relative intensity using 20 nm bins. The error only includes the uncertainty of the detector at 1%. The electrical power measurement error is less than 1%. (For interpretation of the references to color in this figure legend, the reader is referred to the web version of this article.)

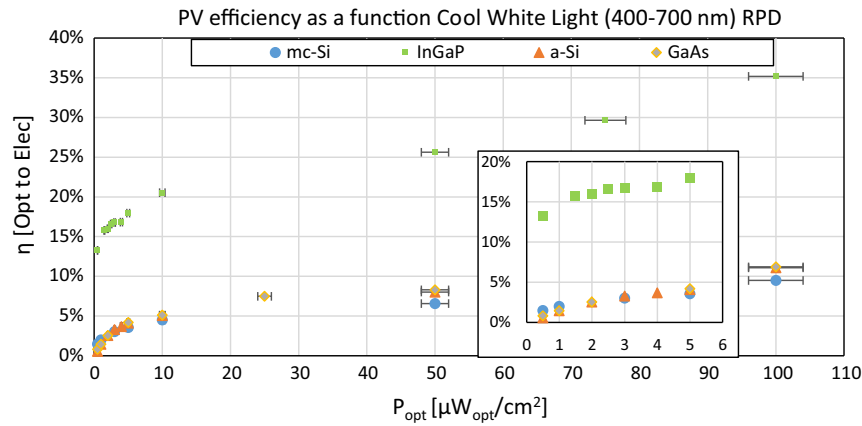


**Fig. 12.** PV conversion efficiency as function of light intensity for the cool white LED. The optical power density error is less than 3% at a 485-nm set wavelength on the optical meter using the bandpass filter binning procedure (2.2 Light Sources and Spectra). The optical power error is 4% including detector uncertainty. The electrical power measurement error is less than 1%.

layer types used in PV packaging processes [42]. The results showed that certain passivation layers have both positive and negative effects on PV efficiency at lower regime conditions. The four tested PV types use  $\text{SiO}_2$  as the anti-reflective coating, which is inexpensive, but not as effective as  $\text{Al}_2\text{O}_3$  for reducing surface recombination. Bulk effects originate from material quality and dopant levels. The device leakage current is a negative byproduct of these fabrication effects. Bulk recombination mechanisms can be reduced by lowering the doping density in the bulk, especially in the emitter and base layer [43,44]. Future work on low light energy harvesting will identify the specific dopant levels of some of the tested homojunction PV cells to maximize power conversion efficiency. The InGaP cell has the highest power conversion efficiency for all three light sources. InGaP cells have a lower leakage current density of  $1.49 \times 10^{-13} \text{ A/cm}^2$ , high EQE over the visible range ( $\sim 90\%$  at 540 nm), and a bandgap of 1.86 eV. InGaP  $\eta$  ranges from 15% to 35% for white light intensity from 1 to  $500 \mu\text{W}_{\text{opt}}/\text{cm}^2$  where typical indoor light ranges from 35 to  $1000 \mu\text{W}_{\text{opt}}/\text{cm}^2$  [34]. GaAs has a higher conversion efficiency than the two Si cells for all three light sources because of less thermalization loss from incident photon energy compared to mc-Si and lower leakage current. GaAs and InGaP have the largest efficiency increase as function of RPD in all three intensity ranges.

### 3.2. Radioluminescence illumination of GaAs and InGaP PV

The two PV cells with the highest efficiency under low-light conditions are compared. The homojunction InGaP cell is selected to be further tested in a beta-photovoltaic cell. Presently, we have designed, constructed, and tested a  $100\text{-}\mu\text{W}_e$  radioisotope battery that uses indirect energy conversion. Commercial off-the-shelf (COTS) gallium arsenide (GaAs) solar cells surround phosphor glass platelets filled with  $^3\text{H}$  gas and convert the low, 530 nm light into DC electrical power. Conversion efficiency from optical to electrical energy is 3%, and total system conversion efficiency is  $\sim 1\%$  (initial nuclear energy of beta decay) [29]. We compared the InGaP cell to the GaAs under RL light at  $\sim 1 \mu\text{W}_{\text{opt}}/\text{cm}^2$  from the  $\text{ZnS:Cu,Al}$  phosphor-lined glass platelets filled with 100 mCi of  $^3\text{H}$  gas at STP.  $I$ - $V$  curves for devices are shown in Fig. 13. The InGaP's  $J_{\text{sc}}$  and  $V_{\text{oc}}$ , due to its higher bandgap, are nearly  $2\times$  more than GaAs. Again, this is due to the decrease in leakage current and thermalization loss (TL). Also, GaAs has  $2\times$  and  $1.6\times$  more TL than InGaP under green and blue illumination shown in Table 3. These magnitudes are calculated by dividing the device bandgap by the peak photon energy. Experimental results and device material properties prove that InGaP is the candidate to replace GaAs for low-light energy harvesting in radioisotope battery.



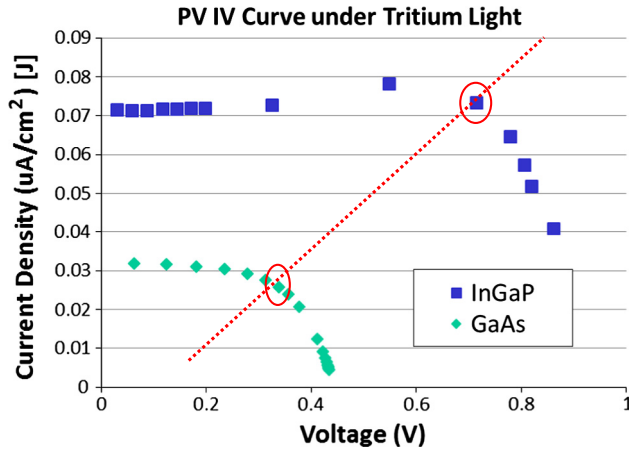


**Fig. 13.** I–V curves of InGaP and GaAs under phosphor-lined tritium platelets at 530 nm. The red dashed line highlights where the maximum power points/surface power densities are for InGaP ( $0.0524 \mu\text{W}_e/\text{cm}^2$ ) and GaAs ( $0.03 \mu\text{W}_e/\text{cm}^2$ ) under 530 nm at a RPD of  $1 \mu\text{W}_{\text{opt}}/\text{cm}^2$ .

### 3.3. Efficiency improvement through optimized incident photon energy

Models have been developed to approximate overall PV conversion efficiency under solar spectrum and monochromatic light. Green et al. proposed a model to calculate the peak conversion efficiency under well-collimated monochromatic light at a high, concentrated light intensity (1000 suns) [45]. PVs are capable of converting under these nonstandard conditions near 100% conversion efficiency dominated by radiative (band-to-band) recombination. The model is limited to photon energies that exceed the PV absorber bandgap under a laser (high intensity and narrow bandwidth). Sze et al. [27,46] and Van Zeghbroeck et al. [47] introduce a first-order model that provides an analytic approximation of PV conversion efficiency for solar spectrum and monochromatic illumination. The ideal efficiency of a single junction photocell under STC, solar spectrum and 1 sun intensity, is 31% for PV  $E_g = 1.35$  eV. The ideal efficiency under Sze's model conditions is 37%. For Van Zeghbroeck's model, the ideal PV cell efficiency is reached at 300 K and an optical concentration of 1000 suns magnitude shown in Eq. (2). The photon energy is ignored or assumed equal to the device bandgap. These models do not apply to low-light conditions, nor narrow spectrum illumination from a LED or phosphor.

$$\eta = \frac{I_{ph} V_m}{P_{in}} = \left[ 1 - \frac{2kT}{E_g} \ln \left( 1 + \frac{E_g}{kT} \right) \right] \quad (2)$$

$I_{ph}$  is the photocurrent independent of the applied voltage;  $V_m$  is the voltage of the maximum power point (MPP); and  $P_{in}$  is the input power from light source. We modified the ideal monochromatic efficiency model by including the device bandgap. The model is a function of photon energy shown in Eq. (3). For the single-junction cell, the model assumes that photons above the bandgap energy will be absorbed. The model is limited by photon energy

less than the bandgap, since low photon energies mostly transmit through the device without being converted or contribute to usable power production ( $E_\lambda \geq E_g$ ). As the photon energy matches the bandgap, the thermal losses decrease, increasing the conversion efficiency. The maximum conversion efficiency limit for GaAs and InGaP when bandgap matched to the incident photon energy is 85% and 88%, respectively. InGaP's efficiency is greater because of its larger bandgap under monochromatic illumination ( $E_\lambda \geq E_g$ ), thus having a higher  $V_{oc}$  limited by the recombination processes in the cell [48]. The theoretical efficiency limit under solar spectrum is approximately 90% due to Carnot limit with the sun as the hot reservoir and the PV cell as the cold reservoir at 300 K [49–51].

$$\eta = \left[ \frac{E_g}{E_\lambda} - \frac{2kT}{E_g} \ln \left( 1 + \frac{E_g}{kT} \right) \right]; \quad E_\lambda \geq E_g \quad (3)$$

The homojunction InGaP PV cell is illuminated by a monochromator at a constant RPD to further study the characteristics of the selected device and formulate an ideal, single-junction solar cell efficiency model for low-light conditions that are narrow bandwidth. InGaP is selected because it has the lowest leakage current and highest  $V_{oc}$  and  $\eta$  for all three light sources. The device is exposed to monochromatic light ranging from 440 to 700 nm at RPD of  $185 \text{ nW}_{\text{opt}}/\text{cm}^2$ . The main objective of this test is to find the optimal wavelength under non-STC. The optimal wavelength would be matched with phosphor emission for the next betaphotovoltaic cell. We discovered that the maximum  $I_{sc}$  is at 614 nm, not at  $E_g$  (1.86 eV; 665.7 nm). EQE plot of InGaP shows that the most number of charge carriers collected is from 510 to 590 nm where it then starts decreasing closer to the PV cell bandgap. The ratio of electrons generated per incident photons is the highest at 540 nm for InGaP.

The incident photon power is constant. We are only concerned about the power conversion efficiency, since the number photons changes for each laser wavelength. We determine that the optimal incident photon energy for a homojunction PV cell is based on the EQE and TL shown in Eq. (4). Focusing on the TL alone, InGaP's conversion efficiency is higher than GaAs, especially in the visible range between 400 and 700 nm, which are the operating ranges for both indoor and RL light. It is therefore justified that a perfect bandgap match would be the peak conversion efficiency of the PV cell. However, we would be ignoring the spectral response of device, which starts to decrease after 600 nm, refer to Fig. 14. A/W (current/power) calculated by dividing output short circuit current ( $I_{sc}$ ) by input optical power at  $185 \text{ nW}_{\text{opt}}$ . By incorporating the device EQE as a function of photon energy in the modified ideal model, the ideal power conversion efficiency can be calculated. This value is at certain incident photon energy that agrees with experimental results shown in Fig. 15. The formulated model shows an optimal wavelength for InGaP at 614 nm. This optimal wavelength matches with InGaP short circuit and spectral response results.

$$\eta = \left[ \frac{E_g}{E_\lambda} - \frac{2kT}{E_g} \ln \left( 1 + \frac{E_g}{kT} \right) \right] \times \text{EQE}(E_\lambda); \quad E_\lambda \geq E_g \quad (4)$$

**Table 3**

TLs for the 2 PV (InGaP and GaAs) cells and 2 phosphors (530 and 450 nm). The PV-phosphor combination with the lowest TL is InGaP with the 530-nm ZnS:Cu, Al phosphor.

Light sources	nm	eV	GaAs TL	InGaP TL
Green (ZnS:Cu, Al) Phosphor	530	2.34	53%	32%
Ice-Blue (ZnS:Ag) Phosphor	450	2.75	63%	44%
Green LED	523	2.37	40%	20%
Blue LED	470	2.63	46%	28%

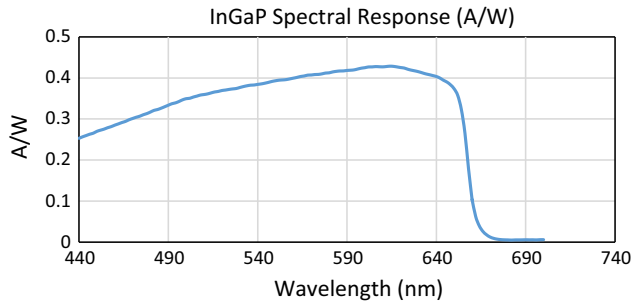


**Fig. 14.** Spectral Response of InGaP at 185 nW<sub>opt</sub>. A/W calculated by dividing output short circuit current ( $I_{sc}$ ) by input optical power at 185 nW<sub>opt</sub>.

If we use the InGaP cell in the current beta-photovoltaic cell, we should use the spectral response and modified model to select a phosphor with a central wavelength matching or close to the optimal wavelength. Current  $^3\text{H}_2$  filled phosphor platelets use ZnS:Ag and ZnS:Cu,Al phosphors because of high CL efficiency and availability. Phosphors such as ZnS:Mn $^{2+}$ , Y $_2\text{O}_3$ :Eu $^{3+}$ , and Y $_2\text{O}_3$ :Eu $^{3+}$  have central emission wavelength closer to the optimal wavelength. However, their cathodoluminescent efficiencies are less than half the efficiency of both ZnS-based phosphors. TL, EQE, and CL efficiency identify the optimal phosphor for the beta-photovoltaic cell system. Using these metrics to calculate the total conversion efficiency, ZnS:Cu,Al is the phosphor choice for the scal-

able and COTS-based beta-photovoltaic cell (Table 4). The total conversion efficiency, also called system efficiency, is assuming the phosphor cathodoluminescent efficiency is equal to radioluminescence efficiency when using an actual radioisotope source.

The spectral characteristics of the device power efficiency determine the photocurrent (Figs. 14 and 15), but one cannot completely compare this to other ideal PV model without incorporating voltage changes. In summary, the model and short-circuit measurements closely approximate the optimal wavelength point for InGaP. The results qualitatively match well with other research work from Bett et al. [48,52], but conversion efficiencies are not identical due to different model assumptions. Bett et al. states that the conversion efficiency peak of InGaP is 47.2% at 610 nm with a laser RPD intensity of 20 W<sub>opt</sub>/cm $^2$ . Their results use the program EtaOpt for theoretical efficiency of device illuminated by a monochromatic light source. EtaOpt is a program code developed at Fraunhofer ISE (<http://www.ise.fraunhofer.de/>) [53]. Using the equation shown in Eq. (4), the efficiency of InGaP is 69.3% at 610 nm. The peak conversion efficiency for InGaP is 69.7% at 614 nm. The equation disregards light intensity, FF, and saturation current ( $J_0$ ). These factors would decrease the efficiency limit. This modified model does not calculate the true overall conversion efficiency of the PV type. Additional factors would be required following EtaOpt program, which is not the major motivation of this report. Nevertheless, the model provides sufficient information by including the device bandgap, EQE, and incident photon energy. Finally, the model identifies the optimal wavelength and phosphor for the InGaP-based  $\beta$ -PV cell.

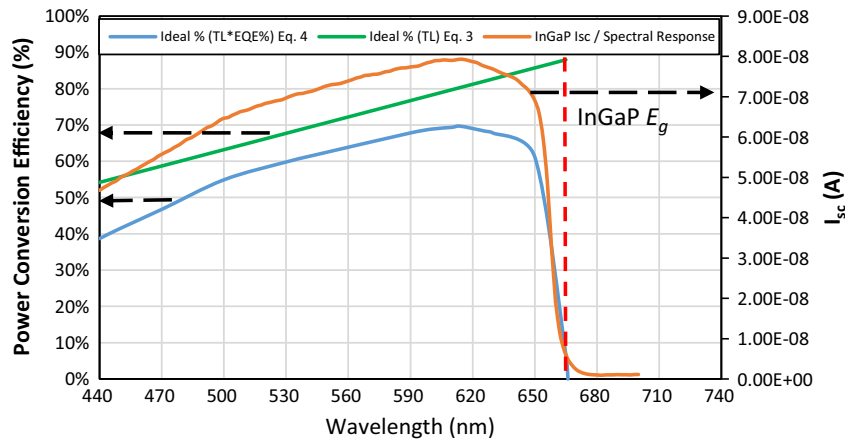


**Fig. 15.** The modified ideal model of the power conversion efficiency qualitatively matches with experimental results of device photo-current under monochromatic light. The optimal wavelength is 614 nm for InGaP even though the bandgap match is at 665.7 nm with a peak power conversion efficiency of 69.7%. This is a theoretical efficiency ignoring device intrinsic losses. This shows that the maximum conversion efficiency is dependent on both device EQE and TL (Fig. 2 for EQE plot of InGaP).

**Table 4**

Ideal system efficiency of different phosphor types. System efficiencies are based on modified ideal model and CL efficiencies.

Phosphor type	Central peak emission (nm)	CL eff. (%)	InGaP ideal eff. (%) at central peak emission	System eff. (%)
ZnS:Ag	450	23 <sup>a</sup>	41.5	9.5
CaS:Ce	525	22 <sup>b</sup>	59.0	12.9
ZnS:Cu, Al	530	22 <sup>a</sup>	59.3	13.0
LaOBr:Tb $^{3+}$	544	20 <sup>a</sup>	61.7	12.3
ZnS:Mn $^{2+}$	590 <sup>c,d</sup>	5.0 <sup>d</sup>	67.8	3.4
Y $_2\text{O}_3$ :Eu $^{3+}$	611	8.7 <sup>a</sup>	69.3	6.0
Y $_2\text{O}_2\text{S}$ :Eu $^{3+}$	626	13 <sup>a</sup>	68.3	8.9

<sup>a</sup> Ref. [36,37].

<sup>b</sup> Ref. [61].

<sup>c</sup> Ref. [62].

<sup>d</sup> Ref. [63].

#### 4. Conclusion

Low light energy harvesting is a key component to fulfil power requirements of ZNE building and remote sensors. For remote sensors, there are limitations with operation time and type of measurement because of the power source's volume and lifetime. Capabilities of sensors powered by a-Si or mc-Si PV cells are limited by low energy density under nonstandard, indoor light conditions. PV cells optimized at an efficiency of  $\sim 25\%$  for solar illumination ( $100 \text{ mW}_{\text{opt}}/\text{cm}^2$ ) suffer reduction in efficiency ( $\sim 2\%$ ) when illuminated at low light ( $1 \text{ } \mu\text{W}_{\text{opt}}/\text{cm}^2$ ) intensity and narrow spectrum. Similar efficiencies can be obtained even under these low-light conditions with homojunction photovoltaic cells whose bandgap closely matches the photon energy, i.e., InGaP device illuminated by  $100 \text{ } \mu\text{W}_{\text{opt}}/\text{cm}^2$  of radiation at 523 nm, 470 nm, or white light (400–700 nm) from an LED has conversion efficiency of near 40%. The InGaP PV cell is at least  $7\times$  more efficient than tested PVs for all 3 light sources at a light intensity of  $1 \text{ } \mu\text{W}_{\text{opt}}/\text{cm}^2$ . The homojunction InGaP PV cell described is the most efficient energy converter under narrow and low light conditions because of the decrease in avoidable losses from surface and bulk effects and unavoidable losses from thermalization losses. InGaP has the lowest leakage current, making it very efficient under these low light conditions. Furthermore, we are able to formulate a modified ideal solar cell model under low monochromatic light conditions, different from the existing model, which is based on  $1000\times$  more light intensity than  $100 \text{ mW}_{\text{opt}}/\text{cm}^2$ . The optimal incident photon energy for InGaP is 2.02 eV ( $\lambda = 614 \text{ nm}$ ). The ideal conversion efficiency is dependent on PV cell thermalization losses and EQE. A phosphor with a central wavelength emission near 614 nm would be the optimal RL emitter for a beta-photovoltaic cell using InGaP. So far, there is no yellow, orange, nor red phosphor with a comparable CL/RL conversion efficiency to ZnS:Cu, Al (2.34 eV) and ZnS:Ag (2.75 eV). ZnS:Cu,Al is selected as the phosphor for the scalable beta-photovoltaic cell because its radioluminescence conversion efficiency at  $\sim 22\%$  and bandgap matching to the InGaP cell. The cool-white LED measurements prove that a  $1\text{-cm}^2$  InGaP PV cell can power a sensor at sleep mode located in dimly lit areas, i.e. room corners, corridors, alleyways or underneath furniture. The narrow light spectrum measurements identify InGaP as the most efficient beta-photovoltaic converter. The InGaP PV cell permits the development of an isotope powered sensor for decade long missions in dark and remote areas. Further development and increased efficiency of InGaP PV cells are necessary for next-generation application such as distributed sensors for environmental monitoring with milliwatt requirements.

#### Conflict of interest

The authors declare that there is no conflict of interest regarding the publication of this article.

#### References

- [1] Kasemann M, Rühle K, Gad KM, Glunz SW. Photovoltaic energy harvesting for smart sensor systems. In: Proc of SPIE, vol. 8763; 2013.
- [2] Yoon S-U, Ghazanfar E, Cheng L, Pamukcu S, Suleimann M. Subsurface event detection and classification using wireless signal networks. *Sensors* 2012;12(12):14862–86.
- [3] Vinel A, Wang L, Yang L, Feng X. Internet of things. *Int J Commun Syst* 2012;1101–2.
- [4] Russo J, Litz M, Katsis D, Brent J, Burns D, Argue R. No.: ARL-TR-7424 Low power radiation detection sensor: architecture for unattended sensing suites. Army Research Laboratory (US), Adelphi (MD); 2015 September.
- [5] Jf R. *Designing indoor solar products: photovoltaic technologies for AES*. Chichester (UK): John Wiley & Sons Ltd; 2005.
- [6] Hande A, Polk T, Walker W, Bhatia D. Indoor solar energy harvesting for sensor network router nodes. *Microprocess Microsyst* 2007;31(6):420–32.
- [7] Weddell A, Harris N, White N. An efficient indoor photovoltaic power harvesting system for energy aware wireless sensor nodes. Pervasive Systems Centre, School of Electronics and Computer Science, University of Southampton, UK; 2008.
- [8] Marszal A. Zero energy building – a review of definitions and calculation methodologies. *J Power Sources* 2006;159:971–9.
- [9] Energy STAR Building Manual: 10. Facility Type K-12 Schools. Energy Star and Department of Energy; November 2006.
- [10] Muller M, Wienold J, Walker WD, Reindl LM. Characterization of indoor photovoltaic devices and light. In: Photovoltaic specialists conference (PVSC), 2009 34th IEEE, Philadelphia; June 2009.
- [11] Randall JF, Jacot J. Is AM1.5 applicable in practice? Modelling eight photovoltaic materials with respect to light intensity and two spectra. *Renewable Energy* 2003;28(12):1851–64.
- [12] Roundy S, Wright PK, Rabaey JM. *Energy scavenging for wireless sensor networks: with special focus on vibrations*. Kluwer Academic Publishers; 2004.
- [13] Steim R, Ameri T, Schilinsky P, Waldauf C, Dennler G, Scharber M, et al. Organic photovoltaics for low light applications. *Sol Energy Mater Sol Cells* 2011;95:3256–61.
- [14] Sacco A, Rolle L, Scaltrito L, Tresso E, Pirri CF. Characterization of photovoltaic modules for low-power indoor application. *Appl Energy* 2013;102:1295–302.
- [15] De Rossi F, Pontecorvo T, Brown TM. Characterization of photovoltaic devices for indoor light harvesting and customization of flexible dye solar cells to deliver superior efficiency under artificial lighting. *Appl Energy* 2015;156:413–22.
- [16] Corazza M, Krebs FC, Gevorgyan SA. Lifetime of organic photovoltaics: linking outdoor and indoor tests. *Sol Energy Mater Sol Cells* 2015;143:467–72.
- [17] Lee HKH, Li Z, Durrant JR, Tsoi WC. Is organic photovoltaics promising for indoor applications. *Appl Phys Lett* 2016;108.
- [18] Matthews I, King PJ, Stafford F, Frizzell R. Performance of III-V solar cells as indoor light energy harvesters. *IEEE J Photovolt* 2016;6(1):230–5.
- [19] Bower KE, Barbanell YA, Shreter YG. In: *Polymers, phosphors, and voltaics for radioisotope microbatteries*. Boca Raton (USA). CRC Press; 2002. p. 210–348.
- [20] Zhi-Heng X, Xiao-Bin T, Liang H, Yun-Peng L, Da C. Development of a beta radioluminescence nuclear battery. *Nucl Sci Tech* 2014;25.
- [21] Wacharasindhu T, Nullmeyer BR, Kwon JW, Robertson JD, Garnov AY. Mechanisms leading to losses in conventional betavoltaics and evolution: utilizing composite semiconductor with infused radioisotope for efficiency improvement. *J Microelectromech Syst* 2014;23(1):56–65.
- [22] Lucheng Z, Hui S. Novel approach for characterizing the specific shunt resistance caused by the penetration of the front contact through the p-n junction in solar cell. *J Semicond* 2009;30(7).
- [23] Zhao J, Dai X, Green M, Wenham S. Improvements in silicon solar cell performance. In: Photovoltaic specialists conference, Las Vegas; 1991.
- [24] Hirst L, Ekins-Daukes N. *Fundamental losses in solar cells*. UK: Department of Physics, Imperial College London; 2009.
- [25] Ekins-Daukes N. Controlling radiative loss in quantum well solar cells. *J Phys D: Appl Phys* 2013;46(26).
- [26] Shockley W, Queisser H. Detailed balance limit of efficiency of p-n junction solar cells. *J Appl Phys* 1961;32(3):510–9.
- [27] Sze S, Ng K. Chapter 13: Photodetectors and solar cells. In: *Physics of semiconductor devices*. Hoboken: John Wiley & Sons Inc.; 2007. p. 663–742.
- [28] Litz MS, Katsis D, Russo J, Carroll JJ. Tritium power source for long-lived sensors. In: *SPIE 9115, Energy harvesting and storage: materials, devices, and applications V*, Baltimore, Maryland, USA; 2014.
- [29] Russo J, Litz MS, Katsis D. Commercial-off-the-shelf (COTS) indirect energy conversion isotope (IDEC) design structure and power management. Report No.: ARL-TR-7158, Adelphi (MD); December 2014.
- [30] Homo Junction GaAs Cell IV Data-1-3733-2. Microlink Devices Inc.; 2014.
- [31] Hubbard DSM. Summary of RIT Low Intensity InGaP Results. NanoPower Research Laboratory, Rochester Institute of Technology, Rochester, NY.
- [32] CBC-PV-02 Photovoltaic Cell: 2-Series Amorphous Silicon Solar Cell. Cymbet Corporation, 2015. [Online]. Available: <<http://www.cymbet.com/pdfs/DS-72-25.pdf>> [accessed 8 August 2015].
- [33] IXOLAR High Efficiency SolarMD SLMD321H09L. IXYS; 2014 [Online].
- [34] Penella-López MT, Forner MG. *Powering autonomous sensors: an integral approach with focus on solar and RF energy harvesting*. Dordrecht: Springer; 2011.
- [35] Applications for SSL. U.S. Department of energy: office of energy efficiency & renewable energy [Online]. Available: <<http://energy.gov/eere/ssl/applications-ssl>> [accessed 23 June 2016].
- [36] Yen WM, Shionoya S, Yamamoto H. *Fundamentals of phosphors*. Boca Raton, FL: CRC Press; 2007.
- [37] Alig RC, Bloom S. Cathodoluminescent efficiency. *J Electrochem Soc: Solid-State Sci Technol* 1977;124(7):1136–8.
- [38] Green MA. *Solar cells – operating principles, technology and system application*. Kensington. Australia: University of NSW; 1992.
- [39] Best research-cell efficiencies. NREL, 13 May 2016 [Online]. Available: <[http://www.nrel.gov/ncpv/images/efficiency\\_chart.jpg](http://www.nrel.gov/ncpv/images/efficiency_chart.jpg)> [accessed 21 June 2016].
- [40] Moon S, Kim K, Kim Y, Heo J, Lee J. Highly efficient single-junction GaAs thin-film solar cell on flexible substrate. *Nature Scientific Reports*; 2016. p. 1–6.

- [41] Eades WD, Swanson RM. Calculation of surface generation and recombination velocities at the Si-SiO<sub>2</sub> interface. *J Appl Phys* 1985;58.
- [42] Ruhle K, Rauer M, Rudiger M, Giesecke J, Niewelt T, Schmiga C, et al. Passivation layers for indoor solar cells at low irradiation intensities. In: *SiliconPV 2012*, Leuven, Belgium; April 2012.
- [43] Ruhle K, Reindl LM, Kasemann M. Energy capture with optimized photovoltaic cells under low lighting conditions. In: *2012 IEEE international conference on internet of things*; 2012.
- [44] Breitenstein O, Bauer J, Altermatt PP, Ramspeck K. Influence of defects on solar cell characteristics. *Solid State Phenom* 2009;156–158:1–10.
- [45] Green MA. Limiting photovoltaic monochromatic light conversion efficiency. *Prog Photovoltaics Res Appl* 2011;9:257–61.
- [46] Sze S. *Physics of semiconductor devices*. New York: Wiley; 1981.
- [47] Zeghbroeck BV. *Principles of semiconductor devices*; 2011. [Online]. Available: <<http://ecee.colorado.edu/~bart/book/book/title.htm>> [accessed 2015].
- [48] Bett A, Dimroth F, Lockenhoff R, Oliva E, Schubert J. III-V solar cells under monochromatic illumination. In: *Specialists conference 33rd IEEE*, San Diego; 2008.
- [49] Efficiency limits; 2015. [Online]. Available: <<http://www.superstrate.net/pv/limit>> [accessed August 2015].
- [50] Baruch P, De Vos A, Landsberg PT, Parrott JE. On some thermodynamic aspects of photovoltaic solar energy conversion. *Sol Energy Mater Sol Cells* 1995;36(2):201–22.
- [51] Marti A, Araujo GL. Limiting efficiencies for photovoltaic energy conversion in multigap systems. *Sol Energy Mater Sol Cells* 1996;43(2):203–22.
- [52] Letay G, Bett A. EtaOpt - a program for calculating limiting efficiency and optimum bandgap structure for multi-bandgap solar cells and TPV cells. In: *17th EC-PVSEC*, Munich; 2001.
- [53] Bett, etaOpt, Fraunhofer ISE; 2015. [Online]. Available: <<http://www.ise.fraunhofer.de/de/geschaeftsfelder/iii-v-und-konzentrator-photovoltaik/themen/iii-v-epitaxie-und-solarzellen/fue-leistungen/simulation/etaopt>>.
- [54] Grady S. Energy harvesting powers wireless sensors. In: *Power manufacturing*, 2nd Quarterly; 2012.
- [55] 5-mm Round LED C513A-WSS/WSN, CREE, [Online]. Available: <<http://www.cree.com/~media/Files/Cree/LED%20Components%20and%20Modules/HB/Data%20Sheets/C513A%20WSN%20WSS%20MSN%20MSS%201042.pdf>>.
- [56] HLMP-Cx1A/1B/2A/2B/3A/3B New 5 mm Blue and Green LED Lamps Datasheet. Avago Technologies. [Online].
- [57] [Online]. Available: <<http://www.mbmicrotec.com/en/>>.
- [58] Ferlauto AS, Ferreira GM, Pearce JM, Wronski CR, Collins RW, Deng X, et al. Analytical model for the optical functions of amorphous semiconductors from the near-infrared to ultraviolet: applications in thin film photovoltaics. *J Appl Phys* 2002;92(5):2424–36.
- [59] Green MA, Emery K, Hishikawa Y, Warta W, Dunlop ED. Solar cell efficiency tables (version 47). *Prog Photovoltaics Res Appl* 2016;24:3–11.
- [60] Shah AV, Meier J, Vallat-Sauvain E, Wyrsh N, Kroll U, Droz C, et al. Material and solar research in microcrystalline silicon. *Sol Energy Mater Sol Cells* 2003;78(1–4):469–91.
- [61] Ronda CR. Ch1: Emission and excitation mechanisms of phosphors. In: *Luminescence: theory to application*. Weinheim: Wiley-VCH; 2008.
- [62] Zhang Z, She J, Chen H, Deng S, Xu N. Laser-induced doping and fine patterning of massively prepared luminescent ZnS nanospheres. *J Mater Chem C* 2013;1:4970–8.
- [63] Yacobi BG, Holt DB. *Cathodoluminescence microscopy of inorganic solids*. New York: Plenum Press; 1990.